

# A Mechanism for the Maintenance of Sharp Tropical Margins

HIROHIKO MASUNAGA

*Institute for Space-Earth Environmental Research, Nagoya University, Nagoya, Japan*

BRIAN E. MAPES

*Rosenstiel School of Marine and Atmospheric Science, University of Miami, Miami, Florida*

(Manuscript received 4 June 2019, in final form 15 January 2020)

## ABSTRACT


The moist deep tropics are typically separated from the drier subtropics by a sharp horizontal gradient of moisture. The physical nature of this tropical margin is investigated by using A-Train satellite observations to reconstruct its composite mean quasi-meridional thermodynamic structure and processes. The margin is defined here as the most poleward position of a specified column water vapor (CWV) threshold along a satellite track. Multiple CWV thresholds are selected from 35 to 60 mm, bracketing the global tropics histogram minimum value of 48 mm. For all margin thresholds, CWV increases equatorward from the subtropics and eventually asymptotically approaches 48 mm far on the tropical side, apparently as a coincidence of composite averaging since values of 48 mm are infrequent as noted above. For all margin thresholds, precipitation peaks on the tropical side and then asymptotically approaches equatorward a value of  $85 \text{ W m}^{-2}$ , equal to the evaporation asymptote. For the 48-mm threshold, total diabatic forcing of the air column (radiative heating plus surface latent and sensible heat fluxes) changes sign from positive on the tropical side to negative in the subtropics, with the main contrast in radiative heating, owing principally to the longwave effect of high clouds. An analytic two-vertical-mode model of equatorward-flowing air columns is fitted from the observations to elucidate the processes in a Lagrangian column transition. The model captures key features of the composite, and suggests that a key process in the abrupt moistening at the margin is bottom-heavy ascent growing upward beneath the deep subtropical subsidence.

## 1. Introduction

Early modern theories of the Hadley circulation (Schneider and Lindzen 1977; Schneider 1977; Held and Hou 1980) were built largely around dry dynamics, with moist processes viewed as secondary or implicit. In the typical cartoon, deep convection is sketched in the ascending branch, with shallow cumuli at the bottom of the descending branch. This schematic view is silent about water vapor. While precipitation needs to prevail in the tropics to balance column moisture convergence implied by the mean ascent, this water-budget balance alone does not give a quantitative estimate of how moist the balanced state must be.

Recent water vapor observations offer a new basis for defining the meteorological boundary of the tropics: a moisture threshold. Mapes et al. (2018) found that the histogram of instantaneous column water vapor (CWV) estimated from satellite microwave measurements is bimodal, with a moist and a dry peak straddling a shallow dip around 48 mm. Sequences of maps show that the 48-mm contour delineates the sharp but meandering and sinuous margin of a *synoptic-scale* moist regime, bounding the occurrence of the much spottier mesoscale precipitating cloud systems, which are shaped in turn by all their local triggering mechanisms. Mapes et al. (2018) also showed that a column of air passing through this margin from subtropics to tropics (the usual case, since planetary flow is convergent into the tropics in the moisture-bearing lower half of the troposphere) exhibits a momentary enhancement of its Lagrangian moistening rate, that is, a rapid moistening within the air column as it enters the tropics across the margin. This surge of column moistening rate near 48 mm explains

---

 Denotes content that is immediately available upon publication as open access.

---

*Corresponding author:* Hirohiko Masunaga, masunaga@nagoya-u.jp

DOI: 10.1175/JAS-D-19-0154.1

© 2020 American Meteorological Society. For information regarding reuse of this content and general copyright information, consult the [AMS Copyright Policy](https://www.ametsoc.org/PUBSReuseLicenses) ([www.ametsoc.org/PUBSReuseLicenses](https://www.ametsoc.org/PUBSReuseLicenses)).

the relative rarity of that value (the minimum in the CWV histogram), and indicates that some systematic mechanism maintains the sharpness of the margin even as horizontal advection restlessly changes its shape and location. We speculate that this maintenance mechanism involves moist convection, but depends on subtle vertical structure issues, and may be an unexploited constraint on parameterization, since climate models get it wrong in diverse ways (Fig. 6 of [Mapes et al. 2018](#)).

How does the sharp 48-mm margin bounding the deep tropics fit with climate notions based on monthly and longer averages? Broadly speaking, high CWV occurs over warm sea surface temperature (SST), and indeed on average the 48-mm definition even agrees quantitatively with the 27.5°C SST (Fig. 3 of [Mapes et al. 2018](#)) definition of the convecting deep tropics in older literature about monthly means ([Graham and Barnett 1987](#)). Although a near-Clausius–Clapeyron relationship holds between CWV and SST in a statistical sense ([Stephens 1990](#)), oceanic heat capacity prevents SST from keeping up closely with the rapidly deforming envelope of humid air columns on a daily basis. Precipitation is even more patchy and sporadic than water vapor, so rainfall is correlated with SST only in gross averages ([Inoue 1990](#); [Kanemaru and Masunaga 2013](#)) compared to its tighter coupling with CWV (e.g., [Bretherton et al. 2004](#); [Peters and Neelin 2006](#); [Holloway and Neelin 2009](#)).

The moist regime of [Mapes et al. \(2018\)](#) thus should be viewed as a synoptic-scale “dynamic tropics” interacting actively with day-to-day weather, which on average feels its oceanic boundary condition and hews to the static tropical margin envisioned by theories of the geographically bound Hadley circulation and mean climate.

This paper, a follow-on study of [Mapes et al. \(2018\)](#), is aimed at understanding why the tropical margin is preferentially found around a CWV of 48 mm, and exploring the mean physical processes that may govern the enhanced moistening rate as air crosses the margin into the tropics. To this end, satellite measurements from a suite of the A-Train instruments (see [section 2](#)) are first composited to analyze the thermodynamic properties of the atmosphere and estimates of thermodynamic budget terms across the margin ([section 3](#)). Then, these observations are interpreted physically in light of a simple conceptual model ([section 4](#)) and the whole findings are summarized in [section 5](#).

## 2. Satellite and ancillary data

This section summarizes the data products analyzed in this work. The *CALIPSO* and *CloudSat* satellites fly closely together in a 0130 and 1330 LT sun-synchronous

orbit as a member of the A-Train constellation. The W-band radar carried by the *CloudSat* satellite provide detailed measurements of the in-cloud structure, complemented by the *CALIPSO* lidar observations of thin clouds including those left undetected by the *CloudSat*. The vertical profiles of cloud cover and radiative heating rate  $Q_R$  are obtained from the 2B-GEOPROF-lidar Release 4 (R04) dataset ([Mace et al. 2009](#)) and 2B-FLXHR-lidar R04 product ([L’Ecuyer et al. 2008](#); [Henderson et al. 2013](#)), respectively. The latest release (R05) of the *CloudSat* data distribution is not yet available for the combined radar-lidar products above at the time of this writing. The AMSR-E instrument aboard the *Aqua* satellite, belonging also to the A-Train, provides CWV, precipitation, SST, and sea surface wind at the 10-m height ( $u_{10}$ ) in the Remote Sensing Systems (REMSS) version 7 daily products. Surface latent-heat flux is estimated with the bulk equation ([Large et al. 1994](#)) forced by the CWV, SST, and  $u_{10}$  from AMSR-E, where near-surface vapor mixing ratio is derived empirically with CWV and SST using a regression equation constructed from TAO buoy array data (see appendix of [Masunaga and L’Ecuyer 2010](#)). Temperature and water vapor soundings are collected from the *Aqua* AIRS AMSU level-2 (AIRS2RET) version 6 product ([Kahn et al. 2014](#)), with any data other than flagged as “best” masked out to assure the quality of estimates.

The present analysis is applied to *CloudSat*–*CALIPSO* orbits and the matched AMSR-E and AIRS nadir observations over global tropical oceans (25°S and 25°N) for 4.5 years from 1 July 2006 to 31 December 2010. This duration covers a major portion of the period of *CloudSat* operation in its full capacity from its launch in 2006 to the spacecraft battery failure in 2011 that later forced the satellite operation into the daylight-only mode. No satellite sensor capable of measuring wind was available during the study period, so horizontal wind is obtained from the ECMWF interim reanalysis (ERA-Interim, hereafter ERAI) data ([Dee et al. 2011](#)) and is interpolated in space and time to *CloudSat*–*CALIPSO* overpasses.

## 3. Composite meridional structure

### a. Compositing method

In [Mapes et al. \(2018\)](#), the mean properties of atmospheric structure across the margin were studied in a composite quasi-meridional plane constructed with an ensemble of A-Train satellite down-track measurements averaged together. This approach is adopted in the present paper with some minor updates. The tropical margin is simply defined as the most poleward latitude

where a *CloudSat*–*CALIPSO* track intersects with the CWV threshold of 48 mm. All the measurements are then composited as a function of down-track distance measured relative to that margin.

The search for the margin begins at the latitude of 25° in each hemisphere and proceeds toward the equator. Some moisture features associated with midlatitude winter storms (“atmospheric rivers” and associated concepts) may be excluded in this way. While the southward search in the Northern Hemisphere ends at the equator if CWV never reaches the threshold, the northward search from south continues up to 5°N. This irregular treatment allows us to detect the southern edge of the ITCZ even when it stays to the north of the equator as is typically the case in the east Pacific and the Atlantic.

The composite cloud structure, presented in Fig. 1a, illustrates a rich low- and high-level cloud cover, as well as a subtler but distinct midlevel peak (Riley and Mapes 2009), equatorward of the margin (negative distance values), contrasting with suppressed free-tropospheric cloudiness on its poleward side except for slightly enhanced cloud cover near the tropopause extending beyond the margin.

The associated ERAI-analyzed cross-margin wind is depicted in Fig. 1b. Since  $v^*$ , the horizontal wind projected onto *CloudSat*–*CALIPSO* tracks, is approximately meridional (the polar orbits are primarily north–south in low latitudes), the pattern may be described as equatorward wind below 700 hPa and mid- to upper-tropospheric poleward wind, as expected for the Hadley cell, with a slight midlevel wiggle fundamental to the tropics (e.g., Fig. 4 of Mapes 2001). Most of the moisture (contoured in Fig. 1b) is concentrated in the lower troposphere, so the horizontal transport of moisture in the composite plane is equatorward (inflowing) on the subtropical side of the margin (positive distances).

The CWV threshold of 48 mm is adopted from Mapes et al. (2018) based only on its distribution minimum in globally pooled CWV data. Rescaling by mean temperature or saturation value (Kuo et al. 2018, 2020) makes clear that 48 mm is not a magic number for precipitation impacts, but rather a climate- and region-dependent one. For simplicity we prefer to retain the observational purity of CWV rather than bring in ancillary data to construct a rescaled moisture metric. We have examined all our results as a function of ocean basin and present only robust results in this paper. Far beyond that slight basin dependence, however, we also explore very different thresholds below, as an illustration of the conditional sampling effects on the composites. In doing so, another arguably special property of values near 48 mm emerges.

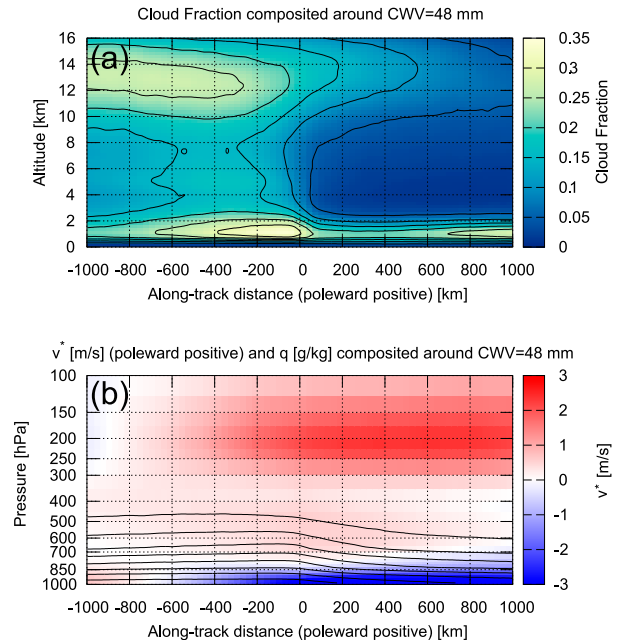


FIG. 1. (a) The vertical structure of cloud cover composited around the 48-mm threshold (shaded and contours). The contour interval is 0.05. (b) The vertical structure of  $v^*$  (horizontal wind projected onto *CloudSat*–*CALIPSO* tracks, shaded) and vapor mixing ratio (contoured every  $2 \text{ g kg}^{-1}$ ) composited around the 48-mm threshold.

### b. CWV, precipitation, and diabatic forcing

CWV monotonically increases equatorward from every threshold used as the composite basis (Fig. 2a), essentially by construction as the threshold-crossing algorithm feels for gradients. Even for high thresholds, precipitation stays weak or virtually absent poleward of the 48-mm value (Fig. 2b). On the equatorward side, all CWV curves gradually asymptotically approach nearly 48 mm, a result that is not at all by construction. It shows a potential hazard of composite averaging, since 48 mm is specifically a PDF minimum (rare value), not a common value in the deep tropics.

Precipitation is always enhanced on the equatorward side of distance zero, even for thresholds of 35 or 40 mm for which the equatorward-side values are well under 45 mm. These may be forced cases, when cool-core midlatitude synoptic eddies intruded into the lower subtropics. Thresholds of 60 mm reveal heavy rain and very sharp gradients, and undoubtedly include tropical cyclones and other intense small-scale weather systems. For precipitation too, an asymptote is approached deep into the tropical side of the composite: a relatively modest value of  $80\text{--}90 \text{ W m}^{-2}$ , which is near radiative–convective equilibrium levels for the global tropics or whole globe. Again, it must be remembered that this is

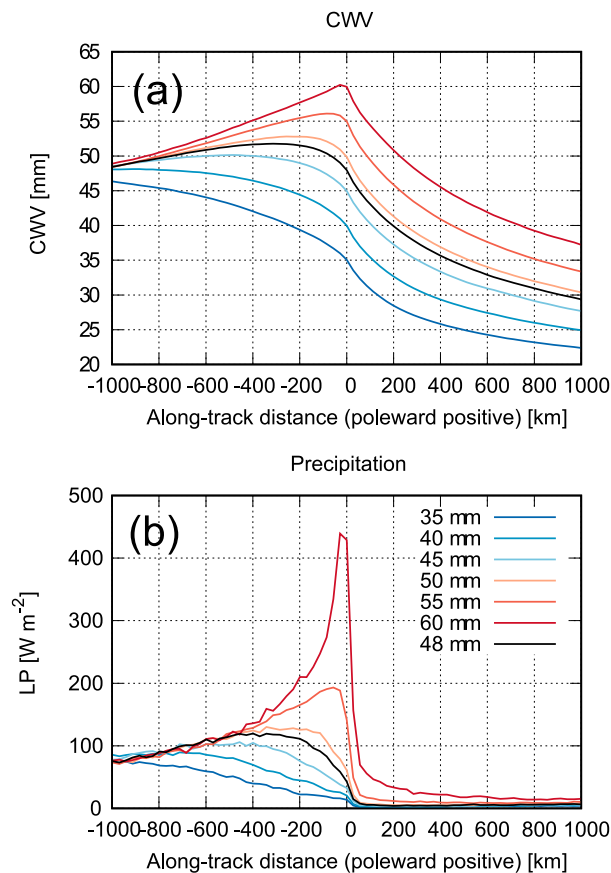


FIG. 2. (a) CWV (mm) and (b) precipitation in ( $\text{W m}^{-2}$ ) composited around various CWV thresholds from 35 to 60 mm in different colors as indicated in the legend in (b). The standard composite plot with the threshold of 48 mm is shown in black.

an average over many situations, including cold tongues on the equatorial side of moist intertropical convergence zones that can be narrower than 1000 km at some longitudes and times. Still, this figure suggests that the moistest air and heaviest precipitation may tend to be found at the periphery of tropical moist air masses, not quite randomly within them as suggested by Allen and Mapes (2017).

In summary, for all thresholds used as a composite key, CWV and precipitation appear to asymptotically approach universal values of 48 mm and  $\sim 85 \text{ W m}^{-2}$ , respectively, in the deep tropics. Is this a coincidence of conditional sampling and averaging, or something more physically determined? The extreme closeness of the lines at the left-hand edge of Fig. 2 makes the latter seem plausible. To further explore possible physical reasons for these numbers, based on modern diabatic views of tropical circulations as opposed to the geographically constrained Hadley cells, the atmospheric energy balance is analyzed in this composite space (Fig. 3).

Total diabatic heating of an air column (Fig. 3a) is defined as the sum of surface latent heat flux (LHF; Fig. 3b), column radiative heating (Figs. 3c,d), and surface sensible heat flux (fixed at  $10 \text{ W m}^{-2}$  for simplicity). Here the 48-mm threshold is indeed special: the composite curves of total diabatic heating differs in character between lower and higher groups of the CWV threshold. For the lowest CWV threshold (35 mm), the atmosphere loses net thermal energy across almost an entire section of the composite space, and even for 45 mm the value is negative inside the humid side of the margin. High threshold values are associated with net heating peaked around distance zero and extending well into the dry side. Suppressed longwave cooling as well as increased shortwave heating, making a qualitative distinction to the low-threshold composites, are the major terms governing the spatial structure of the high-threshold result. These radiative effects are brought about primarily by cirrus clouds as visually evident in Fig. 1 and to a minor extent by water vapor itself (Masunaga and Bony 2018). LHF shows much less structure, aside from providing distinctive enhancements on the dry side of the lowest thresholds.

For an intermediate CWV threshold of 48 or 50 mm, total diabatic forcing vanishes very nearly at distance zero, being positive toward the equator and negative toward the pole. This adds a thermodynamic budget dimension to the histogram-based assertion that the 48-mm CWV value of Mapes et al. (2018) traces out a meaningful regime boundary.

The deep tropical mean LHF (near  $-1000 \text{ km}$  in all composites), and the standard (48 mm) composite of LHF averaged over distances  $< 0$ , is found to be about  $86 \text{ W m}^{-2}$ , very close to the asymptotic value of tropical precipitation seen above. On average, precipitation far on the tropical side of the margin is almost exactly balanced against evaporation in these atmospheric water budget data.

### c. Linking budgets to vertical motion

The diabatic forcing terms as presented in Fig. 3 are instrumental in characterizing moist tropical atmospheric dynamics (Neelin and Held 1987). In this subsection, observations of terms in the CWV and column moist static energy (CMSE) budget are transformed into the two coefficients of a two vertical mode truncation of a diabatic vertical velocity  $\omega_d$ , for use in the analytic model of the next section. This  $\omega_d$  is defined to maintain constant temperature by balancing physically heating and cooling processes through (it is assumed) vertical advection of the composite mean vertical gradients.

This derived  $\omega_d$  could be viewed as an independent estimate of actual atmospheric vertical motion, which is

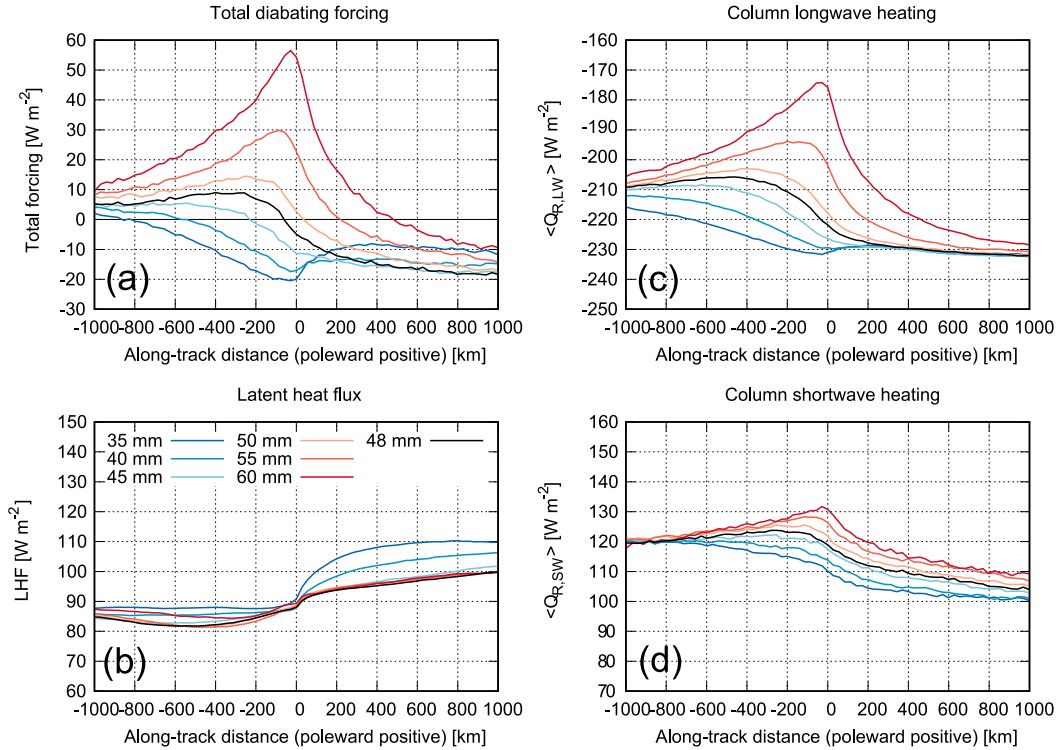


FIG. 3. (a) Total diabatic forcing, (b) surface latent-heat flux, (c) column longwave heating, and (d) column shortwave heating ( $\text{W m}^{-2}$ ) composited around various CWV thresholds from 35 to 60 mm in different colors as indicated in the legend in (b). The standard composite plot with the threshold of 48 mm is shown in black.

weakly constrained on these scales in reanalyses. However, since the basis set of modes utilized is nonunique, and advection of composite gradients by composite  $\omega$  is a crude treatment of vertical transport, it is better to regard this more abstractly as a two-parameter truncation, reflecting thermodynamic considerations alone.

In the real zonal mean Hadley cell, denoted by square brackets,  $[\omega]$  satisfies mass continuity with  $[v]$ , which is purely divergent, while  $[u]$  is purely rotational. Thus  $[v]$  and  $[\omega]$  are strongly constrained by the angular momentum budget on  $[u]$ , and low-level  $[v]$  flowing into the tropics is confined to the near-surface layer upon which zonal surface stress acts. While our composite is only over ocean, and has a meandering latitudinal center point, it has aspects of a zonal mean, and composited ERAI  $\omega$  does exhibit such sharply bottom-intensified vertical structure (Fig. 4) for both 48- and 60-mm thresholds, satisfying mass continuity with the surface-intensified composite  $v$  seen in Fig. 1b.

Nevertheless, the qualitative tilted shape of our two-mode  $\omega_d$  profiles (estimated as detailed below) remains meaningful. Because of the very different vertical gradients of moisture (monotonic) and moist static energy (MSE; reversing with height), the two components of vertical motion—the strength of a deep-layer mean, and a

vertical dipole governing top-heaviness versus bottom-heaviness of the profile—span a space relevant to true profiles of  $\omega$ . These mean gradients are so robust that the simplifying assumptions below (products of composite variables; neglect of eddies) are merely quantitative errors, not qualitative.

Our estimation of a two-mode  $\omega_d$  flows from vertically integrated conservation laws under a steady-state assumption appropriate for time averages, neglecting eddy correlations for simplicity. For specific humidity  $q$  (i.e.,  $\partial_t \equiv 0$ ),

$$\langle \bar{\omega}_d \partial_p \bar{q} \rangle = - \langle \bar{\mathbf{v}} \cdot \nabla \bar{q} \rangle + E - P, \tag{1}$$

while for dry static energy  $s$ ,

$$\langle \bar{\omega}_d \partial_p \bar{s} \rangle = - \langle \bar{\mathbf{v}} \cdot \nabla \bar{s} \rangle + S + \langle Q_R \rangle + LP. \tag{2}$$

Here the overbar denotes the composite averages displayed above (omitted in equations hereafter for simplicity), and  $\langle \dots \rangle$  represents vertical integral over the whole mass of the atmosphere. Variables  $E$  and  $P$  denote surface evaporation and precipitation,  $S$  is surface sensible heat flux,  $L$  is the latent heat of vaporization,  $Q_R$  is net radiative heating rate, and other variables and



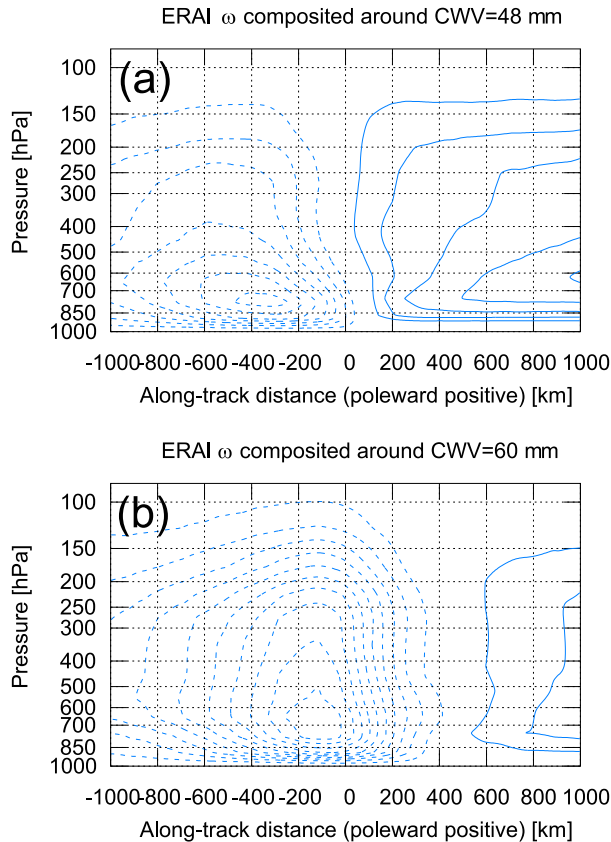


FIG. 4. The composite vertical profile of ERAI  $\omega$  ( $\text{hPa h}^{-1}$ ) for (a) the 48- and (b) the 60-mm thresholds, contoured with an interval of  $0.25 \text{ hPa h}^{-1}$  in solid lines where positive and dashed where negative.

symbols are in standard notation. Eddy correlations between velocity and thermodynamic variables are neglected in the use of “apparent advection” (Yanai et al. 1973), with averaging applied before multiplication, an approximation that is arguably more modest than the ambiguities around vertical basis functions as explained below.

Equation (1) diagnoses vertical moisture advection on the lhs from the rhs terms, which are all known in the composite space from satellite measurements and ERAI-based horizontal wind as illustrated in Figs. 1–4.

Figure 5 shows different terms in the moisture and energy budgets. Horizontal moisture advection induces a modest drying tendency as the result of the arid subtropical air transported toward the tropical margin, but swiftly tapers off on its tropical side (or at negative distances). Vertical moisture advection, derived from (1), also tends to dry the subtropical atmosphere, while moistening the tropical air. This picture is confirmed by vertical dry static energy (DSE) advection (Fig. 5b), in which the adiabatic effects of mean vertical

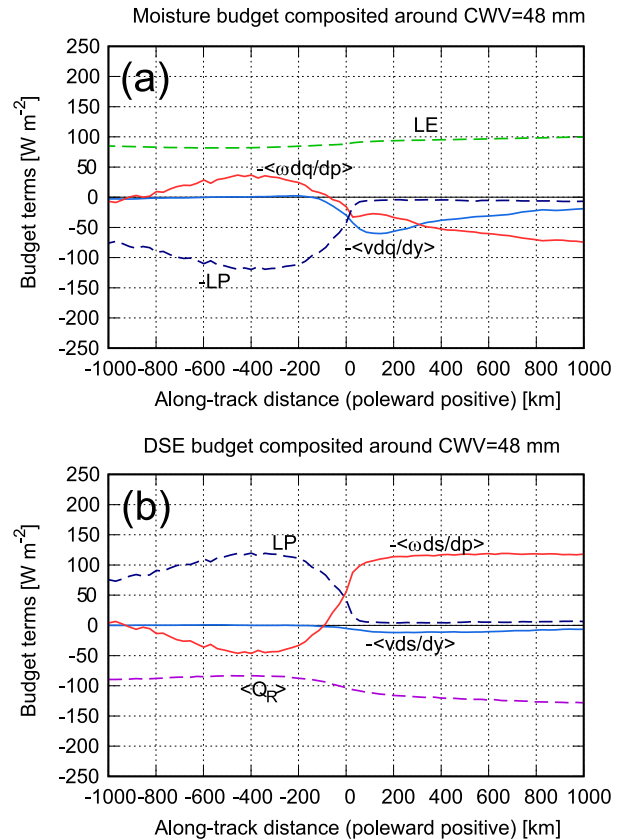


FIG. 5. (a) Moisture budget components ( $\text{W m}^{-2}$ ) in the composite space: vertically integrated horizontal moisture advection (light blue), vertically integrated vertical moisture advection (red), precipitation (dark blue), and evaporation (green). (b) Thermal energy budget components ( $\text{W m}^{-2}$ ) in the composite space: vertically integrated horizontal DSE advection (light blue), vertically integrated vertical DSE advection (red), vertically integrated radiative heating (purple), and precipitation (dark blue). The sign is flipped as necessary so each term has the tendency to increase (decrease) moisture/DSE where positive (negative).

motion balance radiative cooling in the subtropics and convective heating in the tropics.

A two-mode truncation of  $\omega_d$ , following Masunaga and L’Ecuyer (2014), transforms the rhs terms into an estimate of  $\omega$  profiles that satisfy the budget equations. We decompose  $\omega$  into first and second modes,

$$\omega_d(p) = \Omega_1 \hat{\omega}_1(p) + \Omega_2 \hat{\omega}_2(p), \quad (3)$$

where  $\hat{\omega}_i(p)$  denotes the normalized basis function for the  $i$ th mode and  $\Omega_i$  defines the amplitude of each corresponding mode. The vertical advection of moisture and DSE is hence written as

$$\langle \omega_d \partial_p q \rangle = \Omega_1 \langle \hat{\omega}_1 \partial_p q \rangle + \Omega_2 \langle \hat{\omega}_2 \partial_p q \rangle \quad (4)$$

and

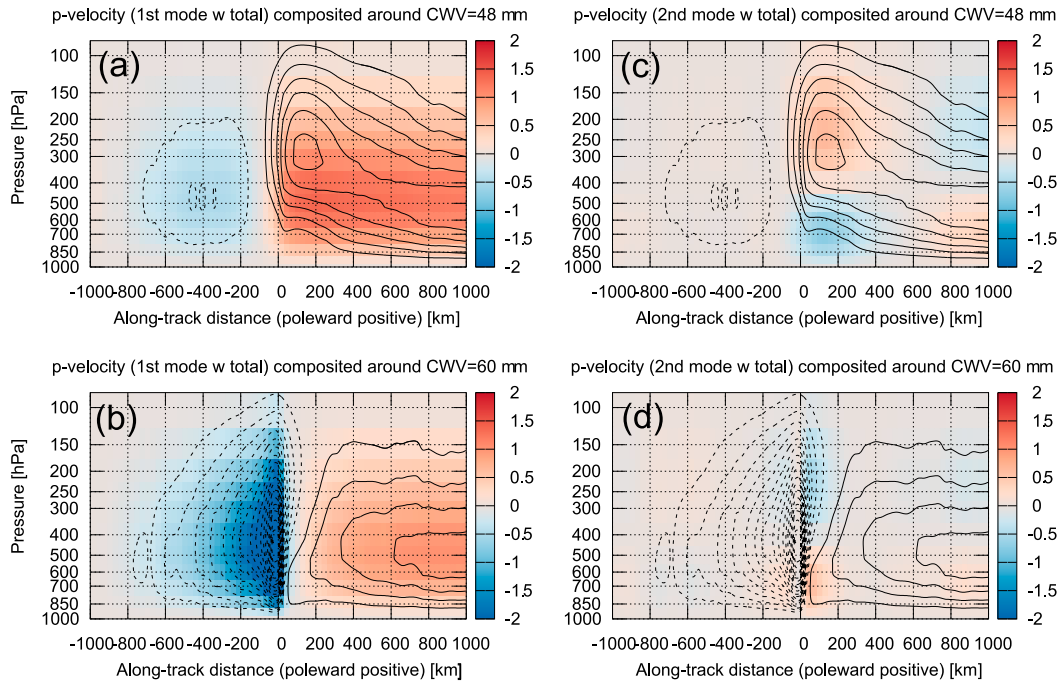


FIG. 6. The composite vertical profile of  $\omega_d$  ( $\text{hPa h}^{-1}$ ) decomposed into the first baroclinic mode (a),(b) and the second baroclinic mode (c),(d) in color shade for two CWV thresholds of (a),(c) 48 and (b),(d) 60 mm. In each panel the sum of the two vertical modes is contoured with an interval of  $0.25 \text{ hPa h}^{-1}$  in solid lines where positive and dashed where negative.

$$\langle \omega_d \partial_p s \rangle = \Omega_1 \langle \hat{\omega}_1 \partial_p s \rangle + \Omega_2 \langle \hat{\omega}_2 \partial_p s \rangle. \quad (5)$$

Equations (4) and (5) constitute a closed system to yield  $\Omega_1$  and  $\Omega_2$  with all other variables being known: the composite profiles of  $q$  and  $s$  are obtained from AIRS soundings, the vertical advection terms on the lhs are diagnosed from (1) and (2), and the basis functions,  $\hat{\omega}_i$ , are adopted from previous work (Masunaga and Sumi 2017).

Those basis functions or vertical modes were computed as the leading (fastest-propagating) dynamical modes of linearized internal wave equations for a realistic tropical static stability profile, in the manner proposed originally by Fulton and Schubert (1985). Such fastest-propagating internal waves are important in small-scale tropical dynamics, because they optimally radiate away the intense quantities of latent heat released in spatially concentrated mesoscale convective systems (e.g., Mapes and Houze 1995). However, they take no account of planetary-scale angular momentum constraints that shape the Hadley cell as discussed above, and thus are not expected to recover the true profiles of  $[v]$  and  $[\omega]$  in the almost-zonal-mean composite of Figs. 1b and 4. Future work could invoke other basis functions, such as empirical maximum covariance modes (EOFs) of  $\omega$ , or the  $\omega$  profiles derived from

leading modes of  $v$ . Since the goal here is merely to establish a two-mode truncation for diagnostic modeling below, errors in the exact vertical spatial structure are secondary, as long as the modes project differently onto the distinct background gradients of  $s$  and  $q$ .

With the basis functions established, complete vertical profiles of  $\omega_d$  can be reconstructed from  $\Omega_1$  and  $\Omega_2$  with (3). This reconstruction procedure is repeated over each atmospheric column from the far subtropics to deepest in the tropics, and displayed in Fig. 6. As expected from the arguments earlier, subsidence (solid contours) dominates to the subtropical side of the margin and weak ascent (dashed contours) prevails to its tropical side. Like the precipitation seen in Fig. 2, diagnosed ascent becomes more intense and sharper as the CWV threshold is increased from 48 mm (Figs. 6a,c) to 60 mm (Figs. 6b,d).

Comparing to the ERAI results in Fig. 4, our mode-based, purely thermodynamically deduced tropical ascent is weaker while subtropical subsidence is stronger for the 48-mm threshold (Figs. 6a,c). When composited against the 60-mm threshold (Figs. 6b,d), the budget-derived  $\omega$  exhibits a confined, intense updraft corresponding to the sharp precipitation peak, while such sharpness is absent in the ERAI tropical ascent. This discrepancy may show the challenges of reanalysis

models for vertical velocity at fine scales, given that ascent in the tropical (nonrotating) atmosphere is theoretically expected to be tightly constrained by precipitation. There is a lot of interproduct spread in different reanalysis tropical  $\omega$  profiles, which often differ even qualitatively (Back and Bretherton 2006; Zhang et al. 2008; Handlos and Back 2014; Huaman and Schumacher 2018). Specifically, Huaman and Takahashi (2016) found that the ERAI tends to exaggerate the bottom-heaviness in the  $\omega$  profile, consistent with the discrepancy in the present comparison. Might model moist physics schemes systematically lack some mechanisms near sharp margins in the CWV field (a state variable that does tend to be well analyzed), potentially making the present observations a usefully discriminating input to model development?

Another remarkable feature of the 48-mm  $\omega_d$  composite in Fig. 6 is the meridional gradient of the second-mode  $\omega_d$  to the poleward side of the margin, resulting in a continuous structural transformation from a bottom-heavy subsidence in the far subtropics into a top-heavy one near the tropical margin. A similar structural transformation is discernible also in the ERAI  $\omega$  profile (Fig. 4a). This gradient over the  $y > 0$  subdomain in the diagnosed  $\omega_d$  profile is rooted in the  $y$  dependence of  $\bar{s}$ ,  $\bar{q}$ , and the column-mean terms on the rhs of (1) and (2), but in vertically nonlocal ways that are not quite easy to attribute.

The matrix inversion behind these  $\omega$  estimates propagates the information content and errors intrinsic to the input observations into the diagnosed results in a way that is not quite intuitively obvious, and depends on the specifics of the basis functions used. Despite all these concerns with its literal accuracy in detail, the point of this diagnostic exercise is really to provide a framework for an interpretive analytic model in the next section, and this two-mode truncation suffices for that purpose.

#### 4. A toy Lagrangian model

The satellite data analysis in the previous section suggests that CWV and precipitation are most enhanced near the tropical margin, where an atmospheric moisture- and energy-budget imbalance is seen, asymptotically approaching equilibrium deeper in the composite tropics. To facilitate a physical interpretation of these results, we develop a simple Lagrangian model that envisions a lower-tropospheric air mass traveling from the subtropics into the tropics. Prognostic variables include CWV and CMSE while diagnostic parameters including precipitation and vertical moisture advection are fitted empirically from the results above. This model

is designed to mimic the composite satellite measurements as shown in Figs. 1–6, when the time dimension in the model is mapped to a quasi-meridional spatial axis. The theoretical formulation is described first, followed by an analysis of model results.

##### a. Basic equations

The present model is built upon column integrated prognostic equations for moisture,

$$D_t \langle q \rangle = - \sum_{i=1}^2 \langle \omega_i \partial_p q \rangle + E - P, \quad (6)$$

and MSE ( $h$ ),

$$D_t \langle h \rangle = - \sum_{i=1}^2 \langle \omega_i \partial_p h \rangle + LE + S + \langle Q_R \rangle, \quad (7)$$

where  $D_t \equiv \partial t + \mathbf{v}_{\text{hor}} \cdot \nabla$  denotes an effective horizontally Lagrangian derivative for the column-mean quantities, and vertical motion has been expanded into two internal-wave vertical modes,  $\omega_i = \Omega_i \hat{\omega}_i$ , as done earlier in section 3c. Neglecting changes and advection of  $\langle T \rangle$ , (7) can be rewritten in terms of  $q$  as

$$LD_t \langle q \rangle = L \sum_{i=1}^2 \gamma_i \langle \omega_i \partial_p q \rangle + LE + S + \langle Q_R \rangle, \quad (8)$$

where vertical MSE advection has been substituted by vertical moisture advection using symbol  $\gamma$  for a ratio that is a version of the normalized gross moist stability (GMS) (Neelin and Held 1987; Raymond and Sessions 2007),

$$\gamma_i = - \frac{\langle \omega_i \partial_p h \rangle}{L \langle \omega_i \partial_p q \rangle}, \quad (9)$$

defined separately for each vertical mode. The diabatic forcing terms and GMS are assumed to be functions only of CWV as described later in section 4b.

Two empirical closures are introduced to constrain two remaining unknowns,  $\langle \omega_1 \partial_p q \rangle$  and  $\langle \omega_2 \partial_p q \rangle$ . The first closure hinges on the relative contribution of the vertical monopole and dipole modes in vertical MSE advection; or in other words on a top-heaviness of the  $\omega$  profile:

$$\xi_i = \frac{\gamma_i \langle \omega_i \partial_p q \rangle}{\sum_{i=1}^2 \gamma_i \langle \omega_i \partial_p q \rangle}, \quad (10)$$

where  $\xi_1 + \xi_2 = 1$  by construction. To demonstrate how  $\xi_2$  varies from the subtropics to the tropics, vertical



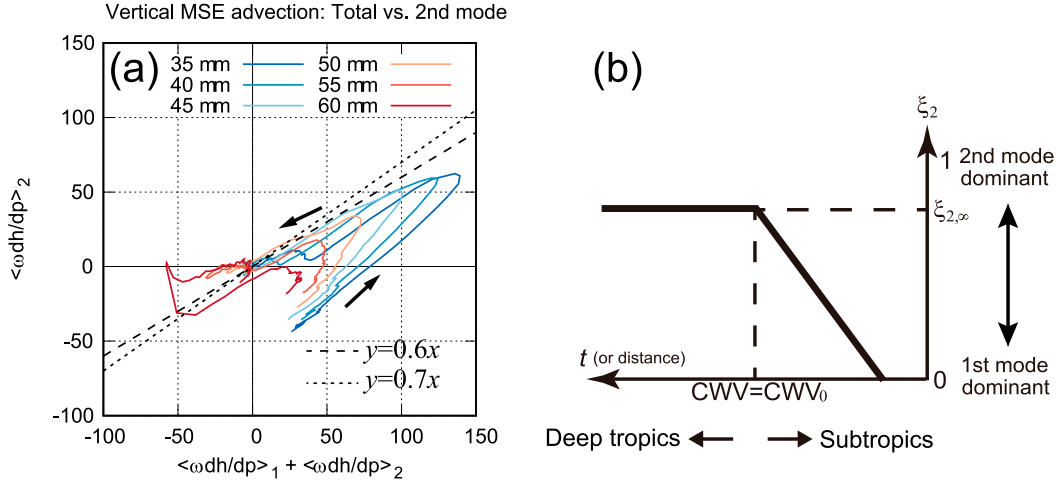


FIG. 7. (a) The composite trajectories of  $\gamma_2 \langle \omega_2 \partial_p q \rangle$  (ordinate) and  $\sum_{i=1}^2 \gamma_i \langle \omega_i \partial_p q \rangle$  (abscissa) for different CWV thresholds. Arrows indicate the equatorward direction along the trajectories. Dashed and dotted lines represent  $\xi_2 = 0.6$  and 0.7 for reference. (b) A schematic model of  $\xi_2$  implied from the observations.  $CWV_0$  refers to the CWV threshold.

moisture advection in the composite space is mapped on the plane of its second-mode component (ordinate) and the total advection (abscissa) in Fig. 7a, where the ratio of the y component to the x component of a given point provides  $\xi_2$ . The trajectories are rooted initially (i.e., on their subtropical end) in the lower-right quadrant and proceed into the upper-right quadrant before making a sharp turn toward the origin. With the exception of the highest CWV threshold, all the composite trajectories are eventually (or to the tropical end) collapsed asymptotically into a slope of  $\sim 0.6$ – $0.7$ . This behavior may be translated in terms of  $\xi_2$  as schematically illustrated in Fig. 7b, showing that  $\xi_2$  increases equatorward until saturated at a certain level designated by  $\xi_{2,\infty} \approx 0.6$  or  $0.7$ .

The second closure is the precipitation inefficiency of Masunaga and Sumi (2017)  $\eta_i$ , defined as the fraction of the column moistening owing to the  $i$ th vertical mode that does not instantly precipitate out. The original form of  $\eta_i$  is generalized for the present model by including a background precipitation  $P_{bg}$ , the precipitation rate that is produced irrespective of large-scale updraft,

$$P = -\sum_{i=1}^2 (1 - \eta_i) \langle \omega_i \partial_p q \rangle + P_{bg}. \quad (11)$$

Precipitation does not occur in association with a column advective drying, so  $\eta_i$  must be precisely unity for  $\langle \omega_i \partial_p q \rangle > 0$ . Otherwise it is known that  $\eta_i$  is modestly variable from around 0.1 to slightly below 0 for the first mode and varies between 1 and  $\sim 0.8$  for the second mode (see Masunaga and Sumi 2017). In other words, the first-mode column moistening is almost entirely converted into precipitation, while the second-mode dynamics is by far less efficient in rainfall production.

Equations (6), (8), (10), and (11) are combined into the diagnostic equation of vertical moisture advection for each vertical mode,

$$L \langle \omega_i \partial_p q \rangle = -\frac{\xi_i}{\gamma_i} (LP_{bg} + S + \langle Q_R \rangle) \left[ \sum_{i=1}^2 \left( 1 + \frac{\eta_i}{\gamma_i} \right) \xi_i \right]^{-1}, \quad (12)$$

and the prognostic equation of moisture,

$$LD_i \langle q \rangle = \left\{ L(E - P_{bg}) + \left[ \frac{\eta_1}{\gamma_1} (1 - \xi_2) + \frac{\eta_2}{\gamma_2} \xi_2 \right] (LE + S + \langle Q_R \rangle) \right\} \left[ 1 + \frac{\eta_1}{\gamma_1} (1 - \xi_2) + \frac{\eta_2}{\gamma_2} \xi_2 \right]^{-1}, \quad (13)$$

where  $\xi_1$  has been eliminated with  $\xi_1 = 1 - \xi_2$ .

*b. Model assumptions*

To complete a prognostic model of moisture, each parameter in the rhs of (13) is prescribed as a function of  $\langle q \rangle$ .

The diabatic forcing terms ( $E$ ,  $S$ , and  $\langle Q_R \rangle$ ) are modeled so they mimic the observations presented in Fig. 3. Surface latent-heat flux varies only to a minor extent in an unsystematic manner with CWV in Fig. 3b and thus is set to a constant at the tropical mean of  $85 \text{ W m}^{-2}$ .

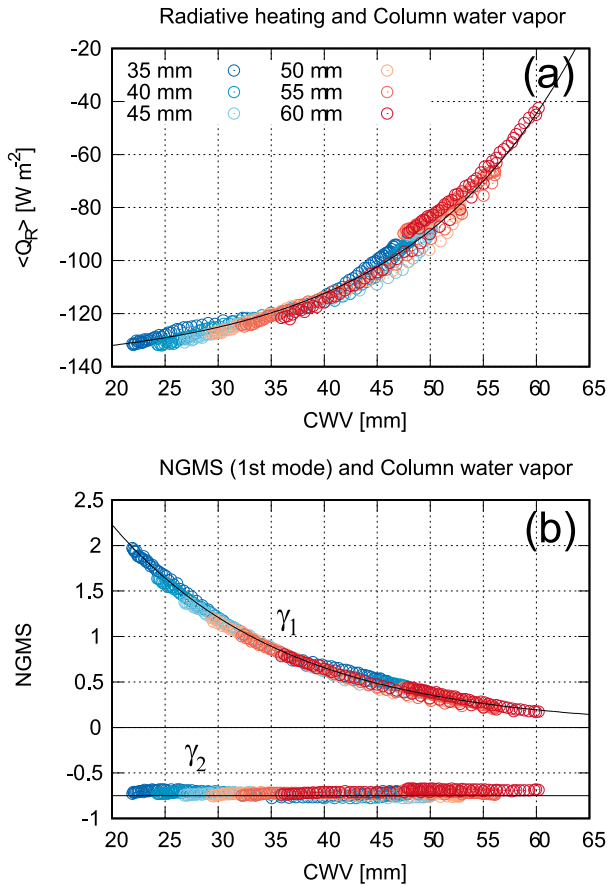


FIG. 8. The composite trajectories mapped on (a) the  $\langle Q_R \rangle$ -CWV plane and (b) the  $\gamma_1$ -CWV plane for different CWV thresholds. The exponential fit to  $\langle Q_R \rangle$  and  $\gamma_1$  as a function of CWV is depicted as a solid curve (see text for fitted coefficients). The reference to  $\gamma_2$  is a horizontal line at  $-0.75$ .

Surface sensible-heat flux is fixed at  $10 \text{ W m}^{-2}$  for the same reason. Column radiative heating, in contrast, is the primary driver of total diabatic forcing, tightly related to CWV mainly through the cirrus radiative effects. Figure 8a shows the observed relationship of  $\langle Q_R \rangle$  with CWV constructed from the composite satellite measurements. The observations imply a surprisingly close coupling between the two parameters, tightly lined up along an exponential curve. The exponential fit to the data is found to be

$$\langle Q_R \rangle = 2.32 \exp(6.19 \times 10^{-2} \langle q \rangle) - 140, \quad (14)$$

for  $\langle Q_R \rangle$  in the units of watts per square meter and  $\langle q \rangle$  in kilograms per square meter (or equivalently millimeters). Total diabatic forcing is thereby formulated as

$$LE + S + \langle Q_R \rangle = 2.32 \exp(6.19 \times 10^{-2} \langle q \rangle) - 45, \quad (15)$$

which vanishes when  $\langle q \rangle = 47.9 \text{ mm}$ , hereafter denoted by  $\langle q \rangle_{\text{eq}}$ , confirming the argument earlier that a CWV of about 48 mm provides the energy budget neutrality. An exponential fit is also successfully applied to the first-mode GMS (Fig. 8b) as

$$\gamma_1 = 7.55 \exp(-6.10 \times 10^{-2} \langle q \rangle). \quad (16)$$

The decrease of  $\gamma_1$  toward zero with increasing CWV is expected from the fact that a low-level import of MSE almost suffices for moist tropical soundings, while far from sufficient in the dry subtropical air, to offset the upper-level MSE export associated with deep ascent. The observations indicate that  $\gamma_2$  is practically independent of CWV and is safely set to a constant at  $-0.75$ .

A set of the CWV thresholds defining the composite base points for Figs. 1–6 are emulated in model runs by switching a “subtropics regime” to a “tropics regime” at a specified CWV value, hereafter denoted by  $\text{CWV}_0$ , in every 5 mm from 35 to 60 mm. The regime transition is controlled by  $\xi_2$  and  $P_{\text{bg}}$ . The schematic illustration in Fig. 7 is adopted to prescribe  $\xi_2$ ,

$$\xi_2 = \begin{cases} \xi_{2,\infty} \left[ 1 + \frac{\text{CWV} - \text{CWV}_0}{\Delta_q} \right] & \text{for } \text{CWV} < \text{CWV}_0 \\ \xi_{2,\infty} & \text{for } \text{CWV} \geq \text{CWV}_0, \end{cases} \quad (17)$$

where  $\Delta_q$  is chosen to be 20 mm. In the subtropics regime ( $\text{CWV} < \text{CWV}_0$ ),  $\xi_2$  is designed to increase with  $t$  according to (17), exploiting the observational fact that CWV persistently rises toward distance zero on its poleward side (Fig. 2) and thus CWV is expected to be monotonically related to  $t$ . The background precipitation,  $P_{\text{bg}}$ , is assumed to obey a step function,

$$P_{\text{bg}} = \begin{cases} 0 & \text{for } \text{CWV} < \text{CWV}_0 \\ E & \text{for } \text{CWV} \geq \text{CWV}_0. \end{cases} \quad (18)$$

This is a simplistic realization of the observation that precipitation is absent in the subtropics, and asymptotically approaches an equilibrium against evaporation in the deep tropics (Fig. 2).

Table 1 summarizes the parameter settings as described above in the top row (control) as well as three additional runs performed to test the sensitivity to some major uncertainties in the model assumptions. The default settings for the control run are  $\eta_1 = 0.1$ ,  $\eta_2 = 1$ , and  $\xi_{2,\infty} \approx 0.6$ . The  $\eta_208$  run is identical to the control run except that  $\eta_2$  is set to 0.8 instead of 1. In the  $\eta_100$  run,  $\eta_1$  is reduced from 0.1 to 0. The selected values for  $\eta_1$  and  $\eta_2$  in these two experiments roughly bound the plausible

TABLE 1. Parameter settings for the conceptual model. A pair of numbers are provided for  $\eta_i$  ( $i = 1$  and  $2$ ) to indicate the cases of  $\langle \omega_i \partial_p q \rangle < 0$  and  $\langle \omega_i \partial_p q \rangle > 0$  in this order.

Run	$LE$ ( $W m^{-2}$ )	$S$ ( $W m^{-2}$ )	$\langle Q_R \rangle$ ( $W m^{-2}$ )	$\gamma_1$	$\gamma_2$	$\eta_1$	$\eta_2$	$\xi_{2,\infty}$
Control	85	10	(14)	(16)	-0.75	(0.1, 1)	(1, 1)	0.6
$\eta_2 = 0.8$	85	10	(14)	(16)	-0.75	(0.1, 1)	(0.8, 1)	0.6
$\eta_1 = 0.0$	85	10	(14)	(16)	-0.75	(0.0, 1)	(1, 1)	0.6
$\xi_2 = 0.7$	85	10	(14)	(16)	-0.75	(0.1, 1)	(1, 1)	0.7

range of each parameter that accounts for observations (Masunaga and Sumi 2017). In the fourth run ( $\xi_{07}$ ),  $\xi_{2,\infty}$  is slightly changed from 0.6 to 0.7 in (17) in order to test the sensitivity to  $\xi_2$ .

c. Model runs

1) SIMULATED RESULTS OF THE CONTROL RUN

Equation (13) is integrated over time to simulate the Lagrangian evolution of  $\langle q \rangle$ , as a simple prognostic model for interpreting the observed meridional variation of CWV as mentioned in the beginning of section 4. The initial condition of CWV is  $CWV_0 - \Delta_q$  so that  $\xi_2 = 0$  at  $t = 0$ . Figures 9a and 9b presents the control simulations of CWV and precipitation, where the time

axis is reversed in direction and all curves are shifted in time so that CWV equals  $CWV_0$  at  $t = 0$  (with a minimal offset for visual clarity). The simulations are hence comparable with the observations in Figs. 9c and 9d for a hypothetical Lagrangian air mass moving equatorward at a constant speed, assuming that the quasi-north-south track of the A-Train satellites may be considered as a steady-state representation of such air masses in the composite space. CWV increases monotonically with time until reaching  $CWV_0$  and then tend to converge, successfully capturing the overall characteristics of the observations. Differences are also evident, however, particularly in the latter stage of the simulated evolution ( $t > 0$ ), where CWV converges too slowly for low values of  $CWV_0$  and somewhat too rapidly for the higher

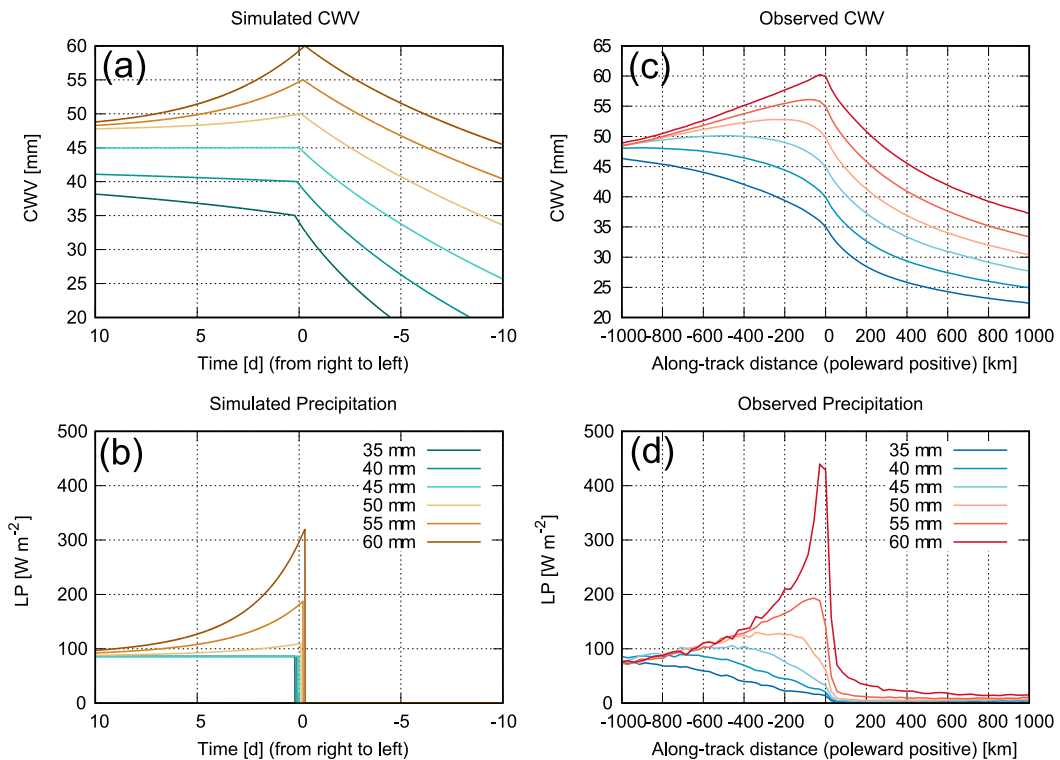


FIG. 9. Control model simulations of (a) CWV and (b) precipitation for different values of  $CWV_0$  as indicated in the legend in (b). Time proceeds from right to left and is defined to be zero when CWV reaches  $CWV_0$ . Different curves are slightly offset in time to avoid visually overlapping together at  $t = 0$ . The observations of (c) CWV and (d) precipitation are shown for comparison, copied from Fig. 2 with the 48-mm composite omitted.

values. The simulations qualitatively reproduce a sharp rise and a subsequent decay of precipitation as found in the observations.

For tracking down the sources of Lagrangian moistening or drying during the evolution, a scale analysis is performed with (13) to measure the moistening time scale  $\tau_q$ :

$$L \frac{\langle q \rangle}{\tau_q} \approx \frac{1}{\mathcal{D}} \left[ L(E - P_{\text{bg}}) + (\mathcal{D} - 1)(LE + S + \langle Q_R \rangle) \right], \quad (19)$$

where

$$\mathcal{D} = 1 + \frac{\eta_1}{\gamma_1} (1 - \xi_2) + \frac{\eta_2}{\gamma_2} \xi_2.$$

Equation (19) implies that the temporal change of CWV is brought about by two factors: an evaporation excess over the background precipitation (the first term on the right), and an energy imbalance (the second term). The moistening rate owing to each component may be estimated by

$$\tau_{q,E}^{-1} \approx \frac{E - P_{\text{bg}}}{\langle q \rangle \mathcal{D}} \quad (20)$$

for the evaporative moistening and

$$\tau_{q,Q}^{-1} \approx \frac{(\mathcal{D} - 1)(LE + S + \langle Q_R \rangle)}{\langle q \rangle L \mathcal{D}} \quad (21)$$

for the energy imbalance. Figure 10 indicates that  $\tau_{q,E}^{-1}$  exceeds  $\tau_{q,Q}^{-1}$  for  $t < 0$  but otherwise  $\tau_{q,Q}^{-1}$  alone accounts for the moistening with  $\tau_{q,E}^{-1}$  totally vanishing. It follows that an air mass is primarily moistened by surface evaporation as it travels toward the equator during the earlier stage of the evolution, while in the latter stage moisture in the air mass is adjusted so the energy imbalance diminishes, either enhanced or reduced depending on the sign of the imposed imbalance. It is noted that the sharp cutoff of  $\tau_{q,E}^{-1}$  in the latter stage results from the simplification that a finite  $P_{\text{bg}}$  is introduced abruptly at  $t = 0$  and thereafter to precisely cancel out evaporation. In reality  $P_{\text{bg}}$  increases smoothly and the evaporative moistening remains to contribute to a certain degree after time 0. A more realistic formulation of  $P_{\text{bg}}$  would thus accelerate the moistening or decelerate the drying for  $t > 0$ , presumably rectifying the awkwardness in the way CWV converges as seen in Fig. 9a. To aid an intuitive interpretation of this awkwardness, (13) can be approximated with the second term on the rhs expanded around the energy equilibrium,

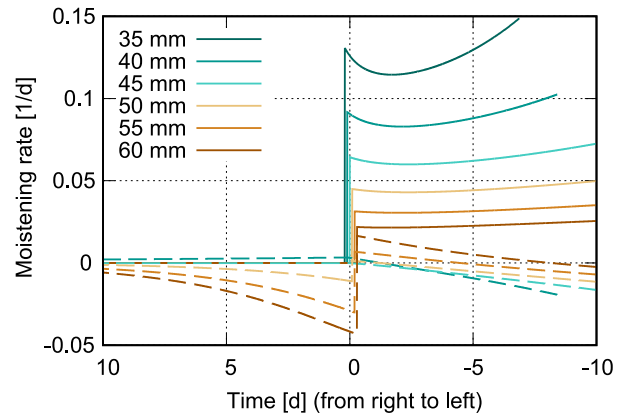


FIG. 10. The moistening rates in the control simulations:  $\tau_{q,E}^{-1}$  (solid) and  $\tau_{q,Q}^{-1}$  (dashed).

$$LD_t \langle q \rangle \approx \frac{1}{\mathcal{D}} \left[ L(E - P_{\text{bg}}) + c_{1,\text{eq}} (\mathcal{D} - 1) (\langle q \rangle - \langle q \rangle_{\text{eq}}) \right], \quad (22)$$

where  $c_{1,\text{eq}}$  is the linear coefficient in the Taylor series of (15). The formal solution of (22) in the absence of the evaporative moistening (i.e.,  $E - P_{\text{bg}} = 0$ ) offers a physical basis for the exponential damping of CWV to the equilibrium value  $\langle q \rangle_{\text{eq}}$  or 47.9 mm as shown earlier. An evaporative moistening present in the course of the damping would act as an external source of moisture, hampering the decay to some degree.

The model provides the vertical mode decomposition of vertical moisture advection by (12). Figure 11 presents the first- and second-mode components of simulated vertical moisture advection (Figs. 11a,b) and their observational counterparts (Figs. 11c,d). The first-mode advection in the model implies a persistent column drying for  $t < 0$  and a following sharp enhancement of column moistening when  $\text{CWV}_0$  is greater than 50 mm, in remarkable agreement with the observations. The second-mode advection has a positive spike just before time 0 with a larger magnitude for a lower value of  $\text{CWV}_0$ . A similar moistening peak is confirmed in the observed second-mode advection. On the other hand, a sudden drying after time 0 apparent in the simulations for  $\text{CWV}_0 \geq 50$  mm is virtually missing in the observations (comparing Fig. 11b and Fig. 11d). This excessive drying in the model is responsible for the aforementioned artifact that CWV is damped too fast when  $\text{CWV}_0$  exceeds the equilibrium value.

## 2) LAGRANGIAN MOISTENING SIMULATED WITH DIFFERENT RUNS

The first-mode dynamics is a main driver of precipitation and the second mode is inefficient in producing

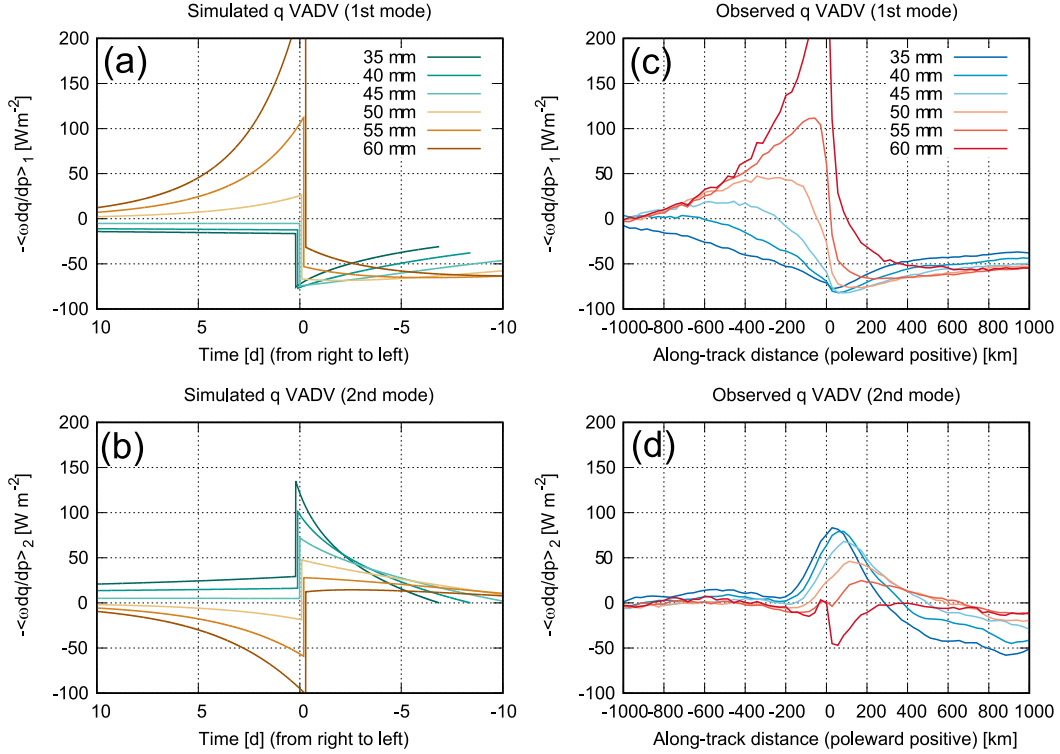


FIG. 11. As in Fig. 9, but for vertical moisture advection: (a) simulated first-mode advection, (b) simulated second-mode advection, (c) observed first-mode advection, and (d) observed second-mode advection.

rainfall under the current model setups (i.e.,  $\eta_1 \sim 0$  and  $\eta_2 \sim 1$ ). The salient enhancement of the first-mode column moistening therefore accounts for the burst of precipitation seen in Fig. 9b. Vertical moisture advection tapers off eventually to zero (Fig. 11), explaining why precipitation decays to  $P_{bg}$ . The moisture accumulated by the second-mode dynamics, on the contrary, is designed not to instantly precipitate out and hence to be left behind in the Lagrangian moisture storage. Figure 12 depicts the evolution of the  $D_t\langle q \rangle$  term from different runs. Qualitative aspects of the evolution resemble the second-mode component of vertical moisture advection as expected, whereas the peak amplitude varies from one simulation to another. The control run (Fig. 11a) produces a pair of relatively modest peaks straddling  $t = 0$ , positive (moistening) for  $t < 0$  and negative (drying) for  $t > 0$ . The drying peak is sharpened if  $\eta_1$  is decreased from 0.1 to 0 (Fig. 11c). The moistening peak appears to be insensitive to the choice of  $\eta_1$  and  $\eta_2$  within a plausible range, but is substantially magnified when  $\xi_2$  is increased slightly from 0.6 to 0.7 (Fig. 11d).

This sharp moistening sensitive to  $\xi_2$  can be understood by examining the behavior of the prognostic moisture equation [(13)] as a function of  $\xi_2$ . The denominator of the rhs,

$$\mathcal{D} = 1 + \frac{\eta_1}{\gamma_1}(1 - \xi_2) + \frac{\eta_2}{\gamma_2}\xi_2, \quad (23)$$

decreases as  $\xi_2$  increases, or as a bottom-heavy subsidence transforms into a top-heavy one, since  $\gamma_1 > 0$  and  $\gamma_2 < 0$ . For typical values of  $\eta_1 = \eta_2 = 1$ ,  $\gamma_1 = 0.5$ , and  $\gamma_2 = -0.75$ ,  $\mathcal{D}$  decreases from 1 to 2/3 with a subtle increase of  $\xi_2$  from 0.6 to 0.7, and would fall to zero for  $\xi_2 = 0.9$ . A modest change to  $\xi_2$  would therefore have the potential to rapidly accelerate the Lagrangian moistening. Equation (23) is rewritten using (9) and (11) to

$$\mathcal{D} = \frac{\langle \omega \partial_p s \rangle - (P - P_{bg})}{\langle \omega \partial_p h \rangle}. \quad (24)$$

In the close vicinity of and to the subtropical side of the margin,  $P - P_{bg} \sim 0$  (i.e., precipitation is hardly fueled dynamically by vertical moisture advection) and hence

$$\mathcal{D} \approx \frac{\langle \omega \partial_p s \rangle}{\langle \omega \partial_p h \rangle}. \quad (25)$$

Equation (25) admits a specific shape of the  $\omega$  profile that would optimize the vertical gradient weights in the numerator and denominator, just like the normalized



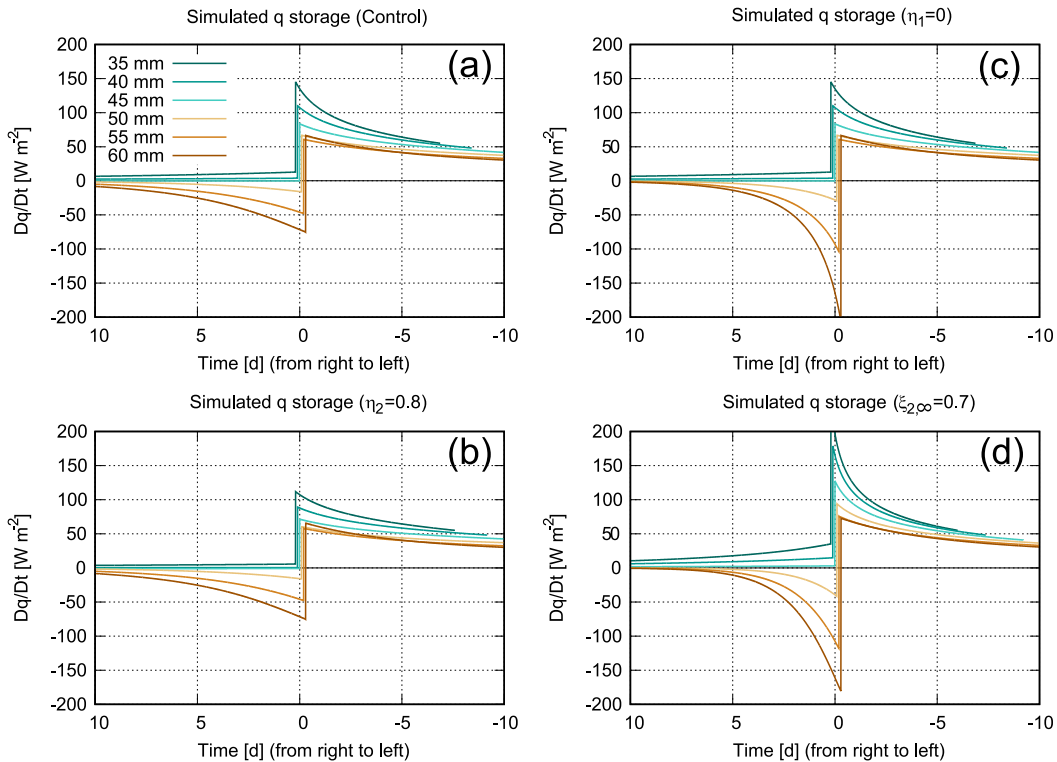


FIG. 12. Simulated Lagrangian moistening,  $D_t\langle q \rangle$  for different model runs: (a) control, (b)  $\eta_2 = 0.8$ , (c)  $\eta_1 = 0.0$ , and (d)  $\xi_2 = 0.7$ . See Table 1 for details of the model setups.

GMS given in (9). The condition of accelerated moistening,  $\mathcal{D} \rightarrow 0$ , is met when the mass integral of vertical DSE advection vanishes, exclusive of the trivial case  $\omega = 0$  at all altitudes. This condition occurs where the subtropical subsidence ( $\langle \omega \partial_p s \rangle < 0$ ) transitions to the tropical ascent ( $\langle \omega \partial_p s \rangle > 0$ ), driven by an increasing contribution of the second-mode shallow updraft. The observations shows that  $\langle \omega \partial_p s \rangle$  indeed intersects the  $x$  intercept near the margin (Fig. 5b). Apart from the mathematical singularity caused by a zero denominator, the sharp spike in  $\langle D_t q \rangle$  presumably offers a qualitative interpretation of the observed Lagrangian moistening at the tropical margin.

## 5. Summary and discussion

This work explores physical processes near the sharp CWV margin observed to encompass the moist tropics as documented in Mapes et al. (2018), which showed a true minimum of the global tropics CWV PDF near a value of 48 mm. Near that value, an enhanced Lagrangian column moistening process is observed, meaning that air columns spend little time at that value, which is what makes its observed frequency of occurrence rare. These relationships are seen in instantaneous data, but the margin moves with time, requiring

a moving composite strategy to localize and quantify the key mechanisms and processes. The ultimate goal of this work is to understand why such rapid moistening tends to occur around the margin.

Observations and retrievals from the A-Train satellite instruments including *CloudSat*, *CALIPSO*, and *AIRS* were analyzed to examine how thermodynamic properties of the atmosphere and energy and water fluxes vary systematically from the subtropical to the tropical side of CWV-threshold defined margins. Millions of individual satellite measurements were averaged into the mean along-track structure of the atmosphere around the margin, defined as the most poleward position of a specified CWV threshold. Six values of the CWV threshold were chosen from 35 to 60 mm to compare with the reference value of 48 mm (the global pdf minimum) from Mapes et al. (2018). The resulting composite observations in the quasi-meridional plane paint out, in a climatological sense, the evolving properties of a lower-tropospheric air mass traveling along the equatorward branch of the Hadley circulation. As a theoretical framework to physically interpret these observations, a two-vertical-mode model closed by  $q$  and  $h$  budgets is developed to prognose the Lagrangian history of moisture within such a traveling air mass.

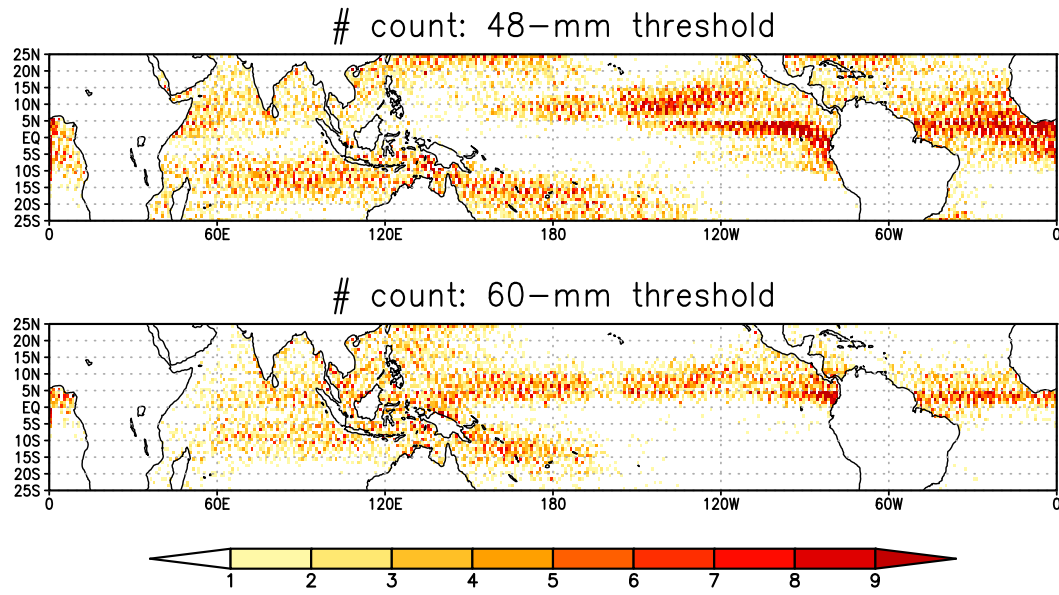


FIG. 13. The globally mapped number count of a specified CWV threshold for CWV = (top) 48 and (bottom) 60 mm. The grid resolution is adjusted to  $1^\circ \times 1^\circ$ .

The observed CWV is found to increase equatorward in the subtropics, but eventually converges to 48 mm in the deep tropics irrespectively of the CWV thresholds. Precipitation intensifies to a peak on the tropical side of the margin and then asymptotically approaches equatorward a value of  $85 \text{ W m}^{-2}$ , almost equal to evaporation. When the CWV threshold for conditional sampling is set higher, a sharper and higher peak emerges as the composite samples rarer and more intense weather situations. An important implication from these results is that the most abundant moisture and precipitation are found not necessarily deepest in the tropics as one might intuitively expect, but instead near margins.

The toy two-mode Lagrangian mathematical model reproduces these key aspects of the observations. In the model, a burst of convection occurs once the air mass passes beyond the margin into the tropics, invigorated by the positivity of diabatic forcing with the aid of a near-zero first-mode GMS. At the same time, however, that enhanced precipitation removes moisture out of the atmosphere, a negatively feedback effect on precipitation through the CWV dependence of radiative heating. Far downstream (deep in the tropics), CWV and precipitation asymptotically approach the balanced climate state. The CWV value for the energy balance neutrality, estimated to be  $\sim 48$  mm, hence serves as the asymptotic value of CWV deepest in the tropics, as well as a CWV minimum in the observed frequency (a rare value). Note that the 48-mm threshold holds only for the global statistics and should be adjusted to the local neutrality criteria when applied regionally. This may partly explain the

known regional dependence of the CWV–precipitation relationship (Bretherton et al. 2004; Kuo et al. 2018).

The behavior described above may be glimpsed in instantaneous satellite images (Fig. 2 in Mapes et al. 2018), but is absent in climatological CWV or rainfall maps because the tropical margins incessantly move and are blurred by Eulerian averaging, leaving behind only slowly varying signals such as the loose connection between convection and the underlying SST (e.g., Gadgil et al. 1984). Figure 13 (top) shows that the 48-mm threshold is found broadly across the tropical and subtropical oceans, except 1) within the Indo-Pacific warm pool (partly because only the most poleward margins are chosen for the CWV threshold along each satellite track), and 2) over cold oceans such as the southeast Pacific and the southern Atlantic. The 60-mm threshold (Fig. 13 bottom), on the other hand, occurs well within the tropical convergence zones, so the composite segments for high threshold values would be tightly drawn around this pattern. It follows that the sharp enhancement of CWV and precipitation near the 60-mm intersection (Fig. 2) mostly occurs deep in the tropics, relaxing swiftly toward the equilibrium (Fig. 2) as does the atmospheric energy imbalance or forcing (Fig. 3). The climatologically moist, rainy tropics of the unconditional mean is hardly static, but rather results from the incessant interplay of budget imbalances and adjustments in mesoscale convective events.

Mapes et al. (2018) found a band of localized column moistening extending along the CWV = 48-mm contour, and showed some satellite cloud-field snapshots.

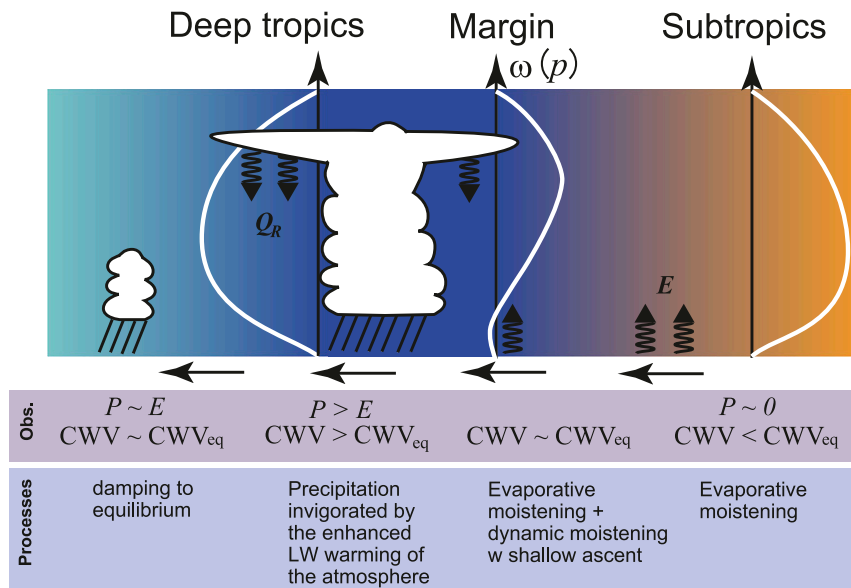


FIG. 14. Schematic summary of the observations and model interpretations.  $CWV_{eq}$  denotes the value giving the energy budget neutrality, corresponding  $\sim 48$  mm for the present tropical climate.

The current model predicts a marked moistening on the subtropical side of the margin in response to increasing  $\xi_2$ , or as the bottom-heavy subsidence in the far subtropics gives way to a bottom-heavy ascent near the margin. The Lagrangian moistening rate from the model diverges to infinity in the limit of  $\langle \omega \partial_p s \rangle / \langle \omega \partial_p h \rangle \rightarrow 0$ , that is, when a lower-tropospheric ascent grows to largely offset the upper-tropospheric subsidence in the vertical integral of  $\omega \partial_p s$ .

The present findings are schematically summarized in Fig. 14. Outstanding questions include how this picture would be modified from region to region. Of particular interest is the east Pacific, where the narrowness of the ITCZ will certainly affect the interpretation of spatial lags of  $\sim 1000$  km for instance. To inquire whether these results (and the model to mimic them) are delicately process dependent, we can look for consistencies or discrepancies in AGCMs and global cloud-resolving models. Two of the three randomly selected climate models studied by Mapes et al. (2018) fail to reproduce the bimodality in the CWV histogram, in diverse ways, suggesting that climate models may lack or miscalibrate the processes essential for the maintenance of sharp margins. Further understanding of those processes may therefore be incisive for diagnosing and ultimately improving the performance of moist process parameterizations in atmosphere models.

*Acknowledgments.* This work is supported by Japan Society for the Promotion of Science (JSPS) Grants-in-Aid

for Scientific Research (KAKENHI) 15KK0157 and 19H01966, as well as by NASA NEWS Program Grant NNX15AD11G and by the National Science Foundation under Grant 1639722.

Data availability statement: The *CloudSat-CALIPSO* data products were provided by the *CloudSat* Data Processing Center (<http://www.cloudsat.cira.colostate.edu>); the AMSR-E products by Remote Sensing Systems (<http://www.remss.com>); the AIRS/AMSU product by the Goddard Earth Sciences (GES) Data and Information Services Center (DISC; <https://disc.sci.gsfc.nasa.gov>); and the ERAI data by ECMWF (<https://apps.ecmwf.int/datasets/>).

## REFERENCES

- Allen, T. L., and B. E. Mapes, 2017: The late spring Caribbean rain-belt: Climatology and dynamics. *Int. J. Climatol.*, **37**, 4981–4993, <https://doi.org/10.1002/joc.5136>.
- Back, L. E., and C. S. Bretherton, 2006: Geographic variability in the export of moist static energy and vertical motion profiles in the tropical Pacific. *Geophys. Res. Lett.*, **33**, L17810, <https://doi.org/10.1029/2006GL026672>.
- Bretherton, C. S., M. E. Peters, and L. E. Back, 2004: Relationships between water vapor path and precipitation over the tropical oceans. *J. Climate*, **17**, 1517–1528, [https://doi.org/10.1175/1520-0442\(2004\)017<1517:RBWVPA>2.0.CO;2](https://doi.org/10.1175/1520-0442(2004)017<1517:RBWVPA>2.0.CO;2).
- Dee, D. P., and Coauthors, 2011: The ERA-Interim reanalysis: Configuration and performance of the data assimilation system. *Quart. J. Roy. Meteor. Soc.*, **137**, 553–597, <https://doi.org/10.1002/qj.828>.
- Fulton, S. R., and W. H. Schubert, 1985: Vertical normal mode transforms: Theory and application. *Mon. Wea. Rev.*, **113**,

- 647–658, [https://doi.org/10.1175/1520-0493\(1985\)113<0647:VNMTTA>2.0.CO;2](https://doi.org/10.1175/1520-0493(1985)113<0647:VNMTTA>2.0.CO;2).
- Gadgil, S., P. V. Joseph, and N. V. Joshi, 1984: Ocean–atmosphere coupling over monsoon regions. *Nature*, **312**, 141–143, <https://doi.org/10.1038/312141a0>.
- Graham, N. E., and T. P. Barnett, 1987: Sea surface temperature, surface wind divergence, and convection over tropical oceans. *Science*, **238**, 657–659, <https://doi.org/10.1126/science.238.4827.657>.
- Handlos, Z. J., and L. E. Back, 2014: Estimating vertical motion profile shape within tropical weather states over the oceans. *J. Climate*, **27**, 7667–7686, <https://doi.org/10.1175/JCLI-D-13-00602.1>.
- Held, I. M., and A. Y. Hou, 1980: Nonlinear axially symmetric circulations in a nearly inviscid atmosphere. *J. Atmos. Sci.*, **37**, 515–533, [https://doi.org/10.1175/1520-0469\(1980\)037<0515:NASCIA>2.0.CO;2](https://doi.org/10.1175/1520-0469(1980)037<0515:NASCIA>2.0.CO;2).
- Henderson, D. S., T. S. L'Ecuyer, G. Stephens, P. Partain, and M. Sekiguchi, 2013: A multisensor perspective on the radiative impacts of clouds and aerosols. *J. Appl. Meteor. Climatol.*, **52**, 853–871, <https://doi.org/10.1175/JAMC-D-12-025.1>.
- Holloway, C. E., and J. D. Neelin, 2009: Moisture vertical structure, column water vapor, and tropical deep convection. *J. Atmos. Sci.*, **66**, 1665–1683, <https://doi.org/10.1175/2008JAS2806.1>.
- Huaman, L., and K. Takahashi, 2016: The vertical structure of the eastern Pacific ITCZs and associated circulation using the TRMM Precipitation Radar and in situ data. *Geophys. Res. Lett.*, **43**, 8230–8239, <https://doi.org/10.1002/2016GL068835>.
- , and C. Schumacher, 2018: Assessing the vertical latent heating structure of the east Pacific ITCZ using the CloudSat CPR and TRMM PR. *J. Climate*, **31**, 2563–2577, <https://doi.org/10.1175/JCLI-D-17-0590.1>.
- Inoue, T., 1990: The relationship of sea-surface temperature and water-vapor amount to convection over the western tropical Pacific revealed from split window measurements. *J. Meteor. Soc. Japan*, **68**, 589–606, [https://doi.org/10.2151/jmsj1965.68.5\\_589](https://doi.org/10.2151/jmsj1965.68.5_589).
- Kahn, B. H., and Coauthors, 2014: The Atmospheric Infrared Sounder version 6 cloud products. *Atmos. Chem. Phys.*, **14**, 399–426, <https://doi.org/10.5194/acp-14-399-2014>.
- Kanemaru, K., and H. Masunaga, 2013: A satellite study of the relationship between sea surface temperature and column water vapor over tropical and subtropical oceans. *J. Climate*, **26**, 4204–4218, <https://doi.org/10.1175/JCLI-D-12-00307.1>.
- Kuo, Y.-H., K. A. Schiro, and J. D. Neelin, 2018: Convective transition statistics over tropical oceans for climate model diagnostics: Observational baseline. *J. Atmos. Sci.*, **75**, 1553–1570, <https://doi.org/10.1175/JAS-D-17-0287.1>.
- , and Coauthors, 2020: Convective transition statistics over tropical oceans for climate model diagnostics: GCM evaluation. *J. Atmos. Sci.*, **77**, 379–403, <https://doi.org/10.1175/JAS-D-19-0132.1>.
- Large, W. G., J. C. McWilliams, and S. C. Doney, 1994: Oceanic vertical mixing: A review and a model with a nonlocal boundary layer parameterization. *Rev. Geophys.*, **32**, 363–403, <https://doi.org/10.1029/94RG01872>.
- L'Ecuyer, T. S., N. B. Wood, T. Haladay, G. L. Stephens, and P. W. Stackhouse Jr., 2008: Impact of clouds on atmospheric heating based on the R04 CloudSat fluxes and heating rates data set. *J. Geophys. Res.*, **113**, D00A15, <https://doi.org/10.1029/2008JD009951>.
- Mace, G. G., Q. Zhang, M. Vaughan, R. Marchand, G. Stephens, C. Trepte, and D. Winker, 2009: A description of hydrometeor layer occurrence statistics derived from the first year of merged Cloudsat and CALIPSO data. *J. Geophys. Res.*, **114**, D00A26, <https://doi.org/10.1029/2007JD009755>.
- Mapes, B. E., 2001: Water's two height scales: The moist adiabat and the radiative troposphere. *Quart. J. Roy. Meteor. Soc.*, **127**, 2353–2366, <https://doi.org/10.1002/qj.49712757708>.
- , and R. A. Houze Jr., 1995: Diabatic divergence profiles in western Pacific mesoscale convective systems. *J. Atmos. Sci.*, **52**, 1807–1828, [https://doi.org/10.1175/1520-0469\(1995\)052<1807:DDPIWP>2.0.CO;2](https://doi.org/10.1175/1520-0469(1995)052<1807:DDPIWP>2.0.CO;2).
- , E.-S. Chung, W. M. Hannah, H. Masunaga, A. J. Wimmers, and C. S. Velden, 2018: The meandering margin of the meteorological moist tropics. *Geophys. Res. Lett.*, **45**, 1177–1184, <https://doi.org/10.1002/2017GL076440>.
- Masunaga, H., and T. S. L'Ecuyer, 2010: The southeast Pacific warm band and double ITCZ. *J. Climate*, **23**, 1189–1208, <https://doi.org/10.1175/2009JCLI3124.1>.
- , and —, 2014: A mechanism of tropical convection inferred from observed variability in the moist static energy budget. *J. Atmos. Sci.*, **71**, 3747–3766, <https://doi.org/10.1175/JAS-D-14-0015.1>.
- , and Y. Sumi, 2017: A toy model of tropical convection with a moisture storage closure. *J. Adv. Model. Earth Syst.*, **9**, 647–667, <https://doi.org/10.1002/2016MS000855>.
- , and S. Bony, 2018: Radiative invigoration of tropical convection by preceding cirrus clouds. *J. Atmos. Sci.*, **75**, 1327–1342, <https://doi.org/10.1175/JAS-D-17-0355.1>.
- Neelin, J. D., and I. M. Held, 1987: Modeling tropical convergence based on the moist static energy budget. *Mon. Wea. Rev.*, **115**, 3–12, [https://doi.org/10.1175/1520-0493\(1987\)115<0003:MTCBOT>2.0.CO;2](https://doi.org/10.1175/1520-0493(1987)115<0003:MTCBOT>2.0.CO;2).
- Peters, O., and J. D. Neelin, 2006: Critical phenomena in atmospheric precipitation. *Nat. Phys.*, **2**, 393–396, <https://doi.org/10.1038/nphys314>.
- Raymond, D. J., and S. L. Sessions, 2007: Evolution of convection during tropical cyclogenesis. *Geophys. Res. Lett.*, **34**, L06811, <https://doi.org/10.1029/2006GL028607>.
- Riley, E. M., and B. E. Mapes, 2009: Unexpected peak near  $-15^{\circ}\text{C}$  in Cloudsat echo top climatology. *Geophys. Res. Lett.*, **36**, L09819, <https://doi.org/10.1029/2009GL037558>.
- Schneider, E. K., 1977: Axially symmetric steady-state models of the basic state for instability and climate studies. Part II: Nonlinear calculations. *J. Atmos. Sci.*, **34**, 280–296, [https://doi.org/10.1175/1520-0469\(1977\)034<0280:ASSSMO>2.0.CO;2](https://doi.org/10.1175/1520-0469(1977)034<0280:ASSSMO>2.0.CO;2).
- , and R. S. Lindzen, 1977: Axially symmetric steady-state models of the basic state for instability and climate studies. Part I: Linearized calculations. *J. Atmos. Sci.*, **34**, 263–279, [https://doi.org/10.1175/1520-0469\(1977\)034<0263:ASSSMO>2.0.CO;2](https://doi.org/10.1175/1520-0469(1977)034<0263:ASSSMO>2.0.CO;2).
- Stephens, G. L., 1990: On the relationship between water vapor over the oceans and sea surface temperature. *J. Climate*, **3**, 634–645, [https://doi.org/10.1175/1520-0442\(1990\)003<0634:OTRBWV>2.0.CO;2](https://doi.org/10.1175/1520-0442(1990)003<0634:OTRBWV>2.0.CO;2).
- Yanai, M., S. Esbensen, and J.-H. Chu, 1973: Determination of bulk properties of tropical cloud clusters from large-scale heat and moisture budgets. *J. Atmos. Sci.*, **30**, 611–627, [https://doi.org/10.1175/1520-0469\(1973\)030<0611:DOBPOT>2.0.CO;2](https://doi.org/10.1175/1520-0469(1973)030<0611:DOBPOT>2.0.CO;2).
- Zhang, C., D. S. Nolan, C. D. Thorncroft, and H. Nguyen, 2008: Shallow meridional circulations in the tropical atmosphere. *J. Climate*, **21**, 3453–3470, <https://doi.org/10.1175/2007JCLI1870.1>.